Original Article

Strength–ductility balance of powder metallurgy Ti–2Fe–2W alloy extruded at high-temperature

Abdollah Bahador [a,*], Ammarueda Issariyapat [a], Junko Umeda [a],
Ridvan Yamanoglu [b], Catalin Pruncu [c,d], Astuty Amrin [e],
Katsuyoshi Kondoh [a]

[a] JWRI, Osaka University, 11-1 Mihogaoka, Ibaraki, 567-0047, Osaka, Japan
[b] Kocaeli University, Engineering Faculty, Metallurgical and Materials Engineering Department, Kocaeli, Turkey
[c] Department of Mechanical Engineering, Imperial College London, Exhibition Road, London, SW7 2AZ, UK
[d] Design, Manufacturing & Engineering Management, University of Strathclyde, Glasgow, G1 1XJ, UK
[e] Razak Faculty of Technology and Informatics Universiti Teknologi Malaysia, Jalan Sultan Yahya Petra, Kuala Lumpur, 54100, Malaysia

ARTICLE INFO

ABSTRACT

This study aims to improve the mechanical properties of a Ti–2Fe base alloy by adding W solute and performing hot extrusion at a high temperature (1000 °C). W was added at 0, 1, 2, and 3 wt% using the powder metallurgy route and homogenization heat treatment. The as-extruded materials predominantly consisted of α phase with different microstructure morphologies; Ti–2Fe and Ti–2Fe–1W contained equiaxed α grains, while Ti–2Fe–2W and Ti–2Fe–3W showed equiaxed + acicular and acicular shape, respectively. Effective grain refinement was obtained in Ti–2Fe–2W (average grain size: ~1.64 μm), which greatly contributed to the strengthening. The solid solution of W was studied with X-ray powder diffraction, where a proportional increment of β lattice constant occurred as the W solute increased in the matrix (Ti–Fe). Additionally, electron backscatter diffraction analysis revealed that the W solution reduced the intensity of the prismatic texture along the extrusion direction. Based on the experimental evaluations, extruded Ti–2Fe–2W alloy exhibited a maximum yield strength of 925 MPa with excellent elongation 30% at room temperature, indicating a remarkable trade-off in strength and ductility.

1. Introduction

Ti alloys, known as advanced materials, have a substantial role in structural and biomedical applications, such as aerospace, energy generation, automotive, and chemical processing industries, as well as prostheses, implants, and sporting goods. Their versatility arises from their low density, high specific strength-to-weight ratio, excellent corrosion resistance, and biocompatibility. However, to extend their application, improvements in mechanical properties, namely, strength, creep resistance, ductility, and workability, are

---

necessary [1,2]. This generally can be achieved either by the solid solution of alloying elements (Ti alloy) or dispersion of hard ceramic particulates in pure Ti to make Ti matrix composites (TMCs) [3,4]. These approaches can be accompanied by thermomechanical processing, which allows for the modification of the microstructure and development of refined equiaxed grains that further enhance the mechanical properties [4]. The fabrication of TMCs can be more complicated than alloying because of a few restrictions. Considering the matrix itself, the main challenge is processing the highly reactive characteristics of Ti with reinforcement particles. However, carbides, nitrides, and borides can be used as reinforcements. Suitable reinforcement materials are limited, owing to the following requirements: chemical compatibility with the matrix, similar density and similar thermal expansion coefficients as those of the matrix [5]. In their comprehensive study, Gorsse et al. [6] claimed that titanium boride (TiB) is the best reinforcement material compared with B_4C, CrB, Ti_5Si, and SiC.

Solid solution strengthening of Ti is widely used, owing to the varieties of alloying elements and the resulting improvement in processability. The factors that need to be taken into account for the solid solution strengthening of Ti alloys are the following:

- The *atomic size* of the alloying element governs the characteristics of solid solution, whether interstitial or substantial. The difference in the atomic sizes of the alloy element and Ti is of significance since a larger atomic size difference has a stronger strengthening effect. Kondoh et al. [7] showed that when a small amount of nitrogen is introduced to commercially pure Ti, the ultimate tensile strength can increase to approximately 1000 MPa.
- Owing to the allotropic behavior of Ti, the effect of solute on the s*tability of α and β phases* is important since each phase has different mechanical properties. If the alloying element is α phase stabilizer (O, N, Al), the transus temperature is raised and the α phase extends to higher

temperatures. If it is a β phase stabilizer (Mo, V, Ta, Nb, Ni, Fe, Cu, Si), the transus temperature decreases, consequently facilitating the β phase formation at lower temperatures [8,9].
- From the viewpoint of *cost-effectiveness*, the cost of alloying elements strongly affects the final cost of the product. Normally, Ti alloys contain expensive alloying elements, but by utilizing of suitable ubiquitous elements (including light elements O, N, H [10,11] and inexpensive elements Fe, Si, Cu [4,12,13]), similar mechanical properties can be achieved as those of the expensive elements Ta, Nb, V, Co [14−16].
- Although the addition of alloying elements increases the strength of Ti, the *volume fraction* of alloying elements is limited since excessive solute additions result in a decline in the ductility and trigger brittleness of the Ti matrix. Therefore, optimization of alloying elements is a significant factor in designing Ti alloys.
- The suitable selection of *processing techniques* allows for a complete solid solution Ti alloy. Physical properties of alloying elements, such as melting point and density, control the fabrication method. For instance, when the melting points and densities of alloying elements and Ti matrix are largely different, conventional casting is not suitable. Therefore, stir casting with multiple re-melting processes or powder metallurgy with heat treatment is the preferred fabrication method to obtain a Ti alloy in which solid solution atoms are distributed uniformly.

The sintering of Ti alloy containing β stabilizers results in two-phase (α + β) formation with a lamellar microstructure that consists of different sizes of α colonies. The colony size of α and the prior β grain size greatly affect the mechanical properties of such microstructure [17]. Smaller α colonies are effective in the impediment of slip bands along prior β grain boundaries, and as a result, an increase in the strength and ductility will occur [18]. Although lamellar (α + β) microstructure promotes the strength and resistance to fatigue
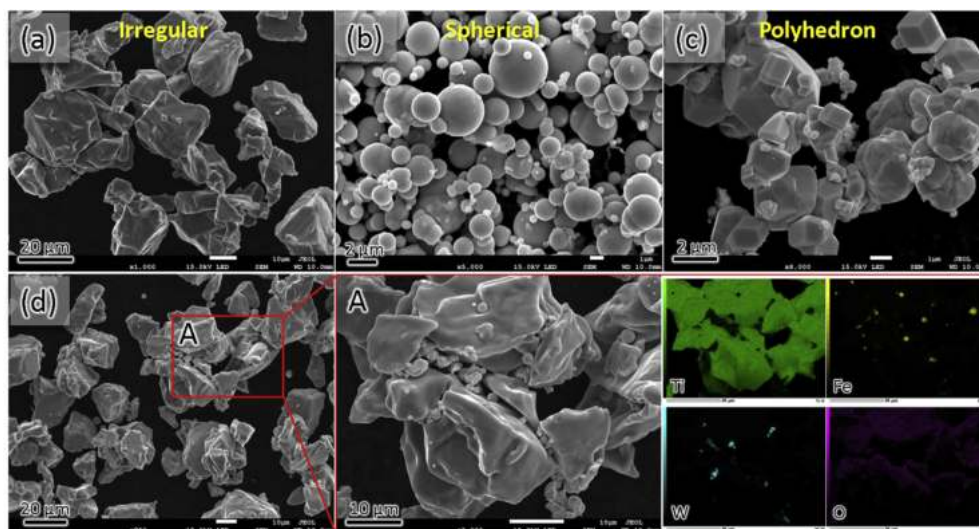

Fig. 1 − FESEM image of raw powders (a) Ti, (b) Fe, and (c) W and (d) premixed powders including high magnification observation.

crack growth, the globular (equiaxed) microstructure facilitates a better strength—ductility trade-off, a desirable factor for many applications of engineering materials [19,20]. Globularized microstructure is generally developed at higher temperatures depending on alloy composition from 815 °C (Ti—6Al—4V) [21] to 1250 °C (Ti—45Al—8Nb—0.2C) [22], and the extrusion temperature governs the microstructure as an essential process parameter. Semiatin et al. [23] showed that the extrusion of Ti—6Al—4V at a lower temperature (815 °C) triggers higher strength in comparison to that at a higher temperature (955 °C) because of the coarse globular microstructure that forms in the latter.

Tungsten (W) and iron (Fe) are β stabilizing elements (substitutional solid solutions in Ti); hence, the microstructure of Ti—Fe—W alloys can contain two-phase constituents (α + β). The fraction of these phases is governed by the amount of the added solutes. W has been generally used as a reinforcement material to improve mechanical and tribological properties of metal matrix composites, such as Al [24], Ti [25] and Cu [26] matrices. W, with its high strength, good thermal conductivity, and high melting temperature [27], is a promising candidate to enhance the mechanical properties of Ti alloys [28]. Therefore, in this study, the effect of W solid solution was studied on the strengthening of extruded Ti—2Fe alloy. The correlation between microstructure and mechanical properties is discussed, and the contribution of solid solution elements along with grain refinement and dislocation density on the tensile strengthening was evaluated quantitatively.

2. Materials and experimental procedure

2.1. Preparation of Ti—2Fe—(0, 1, 2, 3)W alloys

The hydrogenation—dehydrogenation (HDH) process produced pure Ti powder (median particle size of 45 μm), Fe (3—5 μm), and W (2 μm), which were used as raw materials. The micrograph of initial raw powders with different morphologies is shown in Fig. 1. The powders were mixed to make four blends of Ti—2Fe—(0—3)W using a tabletop ball mill (AV-2, Asahi rika Seisakusho) at 100 rpm for a mixing time of 6 h. To disperse the Fe and W uniformly on the Ti powders, ZrO_2 media balls with a diameter of 10 mm were added to the pre-mixed powders. The weight ratio of the powder mixture to the media balls was 5:1. The pre-mixed powders were consolidated employing spark plasma sintering (SPS, SPS-1030S, SPS Syntech Co.) by pouring into a carbon container with an internal diameter of 36 mm and applying uniaxial pressure of 30 MPa under vacuum condition (5 Pa).

The temperature was raised at a rate of 20 °C/min until reaching 1000 °C and then held for 1 h. Due to the large difference in the melting point of W (3422 °C) and Ti (1668 °C), some W particles remained undissolved in Ti—Fe matrix; hence, heat treatment was essential to obtain a complete solid solution. The sintered samples were heat-treated at 1400 °C for 1 h (optimized conditions) in a vacuum atmosphere followed by water quenching. The hot extrusion was applied using a 2000-kN hydraulic press (SHP-200-450, Shibayama Machine Co.) to the homogenized samples to control
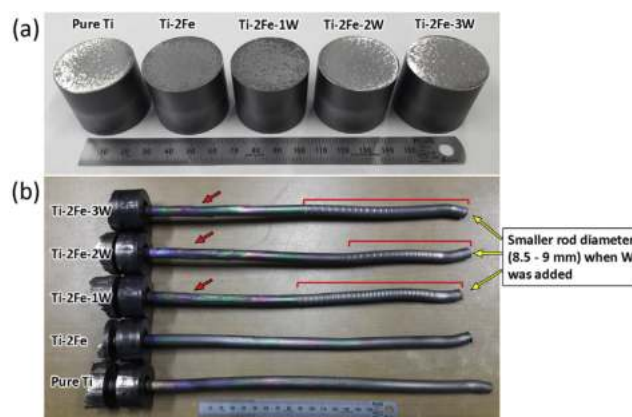

Fig. 2 — (a) As-sintered samples of Ti—2Fe—(0—3)W and (b) corresponding as-extruded rods.

microstructure and eliminate any pores to obtain fully dense specimens. To conduct hot extrusion (considering the container diameter of 37 mm and die hole diameter of 10 mm), the sintered samples were pre-heated to 1000 °C for 5 min in an argon gas atmosphere (5 L/m) at a heating rate of 2 °C/s employing an infrared gold image furnace (RHL-P610C, Advance Riko, Inc.). A hot extrusion ratio of 13 and punch speed of 6 mm/s were used.

The as-sintered and as-extruded materials are illustrated in Fig. 2. The extruded CP-Ti and Ti—2Fe showed a uniform deformation and a smooth surface with a 10-mm rod diameter. In contrast, Ti—2Fe—(1—3)W exhibited nonuniform hot deformation yielding a rough surface and smaller rod diameter (8.5—9 mm). Ti—2Fe—2W showed a better hot extrusion capability among the W-content materials.

2.2. Microstructure characterization and mechanical properties

The samples of microstructure characterization were prepared by mounting small specimens in the carbon resin. The mounted samples were then ground using abrasive papers ranging from 80-to 2000-grit and subsequently buffed with a suspension solution including Al_2O_3 particles (0.05 μm) to obtain a mirror surface. The microstructure was observed using a field emission scanning microscope (FESEM, JSM-6500F, JEOL), and elemental mapping was carried out using energy-dispersive X-ray spectroscopy (EDS; JED-2300, JEOL Ltd.) installed in the FESEM. The images were captured by secondary and backscattered electrons (compo-image) at an acceleration voltage of 15 V.

To evaluate the crystal orientations and textures, electron backscatter diffraction (EBSD) attached to FESEM was employed. The EBSD analysis was carried out using a detector (TSL DigiView IV; EDAX), operated at an acceleration voltage of 15 kV and a tilt angle of 70°. The scanning step size was selected as 0.1 μm. X-ray diffraction (XRD) was performed (Labx, XRD-6100, Shimadzu) to analyze the lattice parameters and phase constituents of the samples, using Cu Kα radiation (wavelength = 1.54178 Å) and a scanning speed of 2°/min.
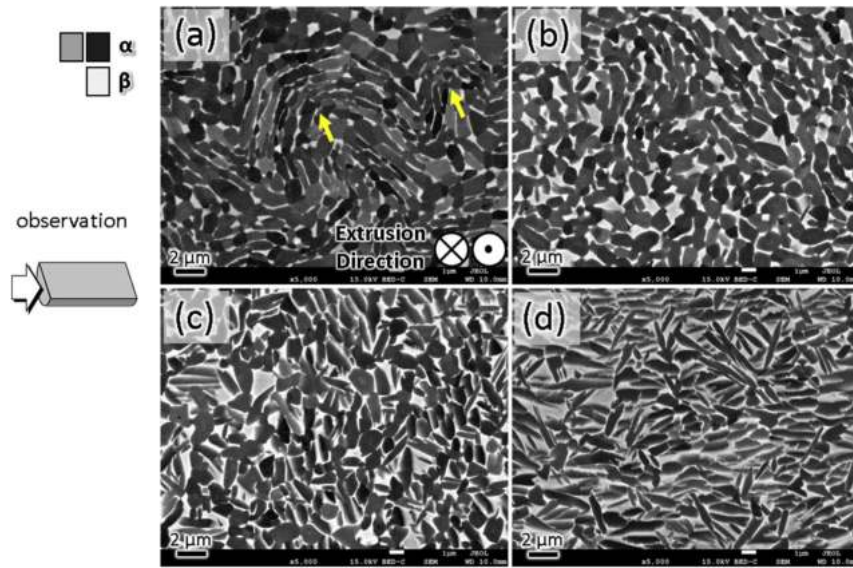
Fig. 3 − FSEM images captured from the direction parallel to the extrusion direction − (a) Ti−2Fe, (b) Ti−2Fe−1W, (c) Ti−2Fe−2W, and (d) Ti−2Fe−3W.

The mechanical properties of extruded samples were evaluated by tensile tests using a universal testing machine (AUTOGRAPH AG-150 KN, Shimadzu) at a nominal strain rate of 5×10^{-4} s^{-1}. The test samples were machined along the extrusion direction with center dimensions of 1×2 mm and a 10-mm gauge length. The displacement was recorded with an advanced digital charge-coupled device camera and a non-contact extensometer system. To guarantee the reproducibility of the tensile test, the measurement was performed using three test samples for each type of alloy investigated.

3. Results and discussion

3.1. Microstructural characterization

Figs. 3 and 4 show the FSEM images of each extruded sample from a different view with reference to the extrusion direction. The microstructure was found to be comprised of two-phase α (dark and grey regions) and β (light grey), where α phase fraction is dominant. Ti−2Fe demonstrates the presence of strong kinks (shown by yellow arrows), including
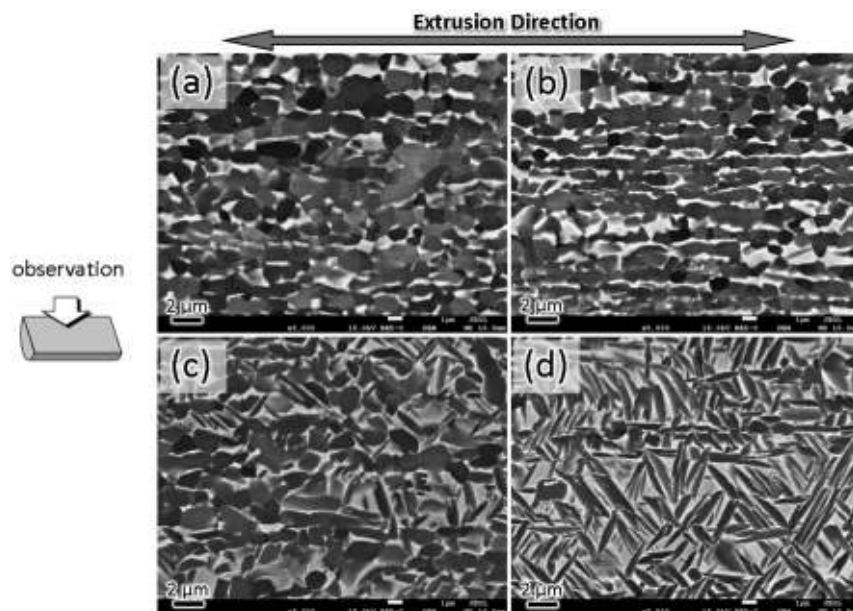

Fig. 4 − FSEM images captured from the direction perpendicular to the extrusion direction − (a) Ti−2Fe, (b) Ti−2Fe−1W, (c) Ti−2Fe−2W, and (d) Ti−2Fe−3W.
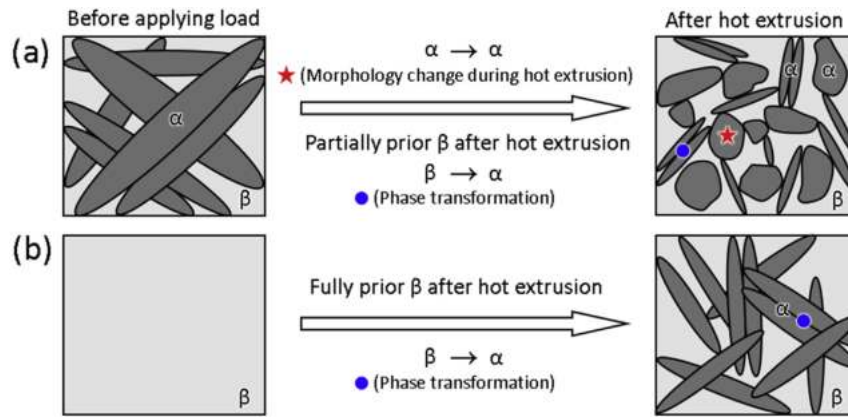
Fig. 5 – Schematic illustration of different α phase morphologies during extrusion. (a) Ti–2Fe–2W: acicular α changes to equiaxed shape during extrusion and partially remained β phase after hot extrusion can transform to small acicular α. (b) Ti–2Fe–3W: the microstructure is fully β phase before applying the load, through unloading, then the acicular α nucleates from metastable β phase during cooling.
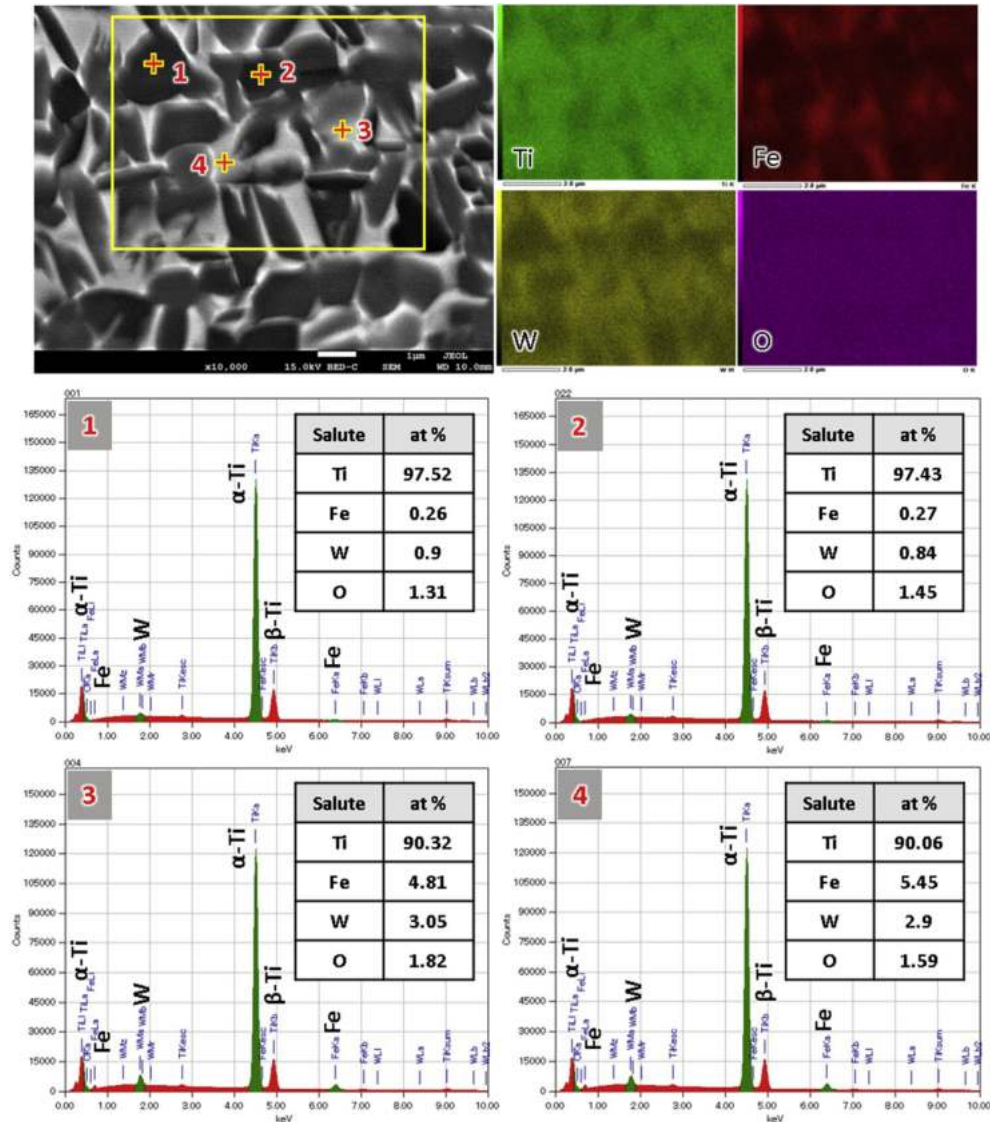

Fig. 6 – Distribution of elements in extruded Ti–2Fe–2W using EDS qualitative mapping and quantitative point analysis.
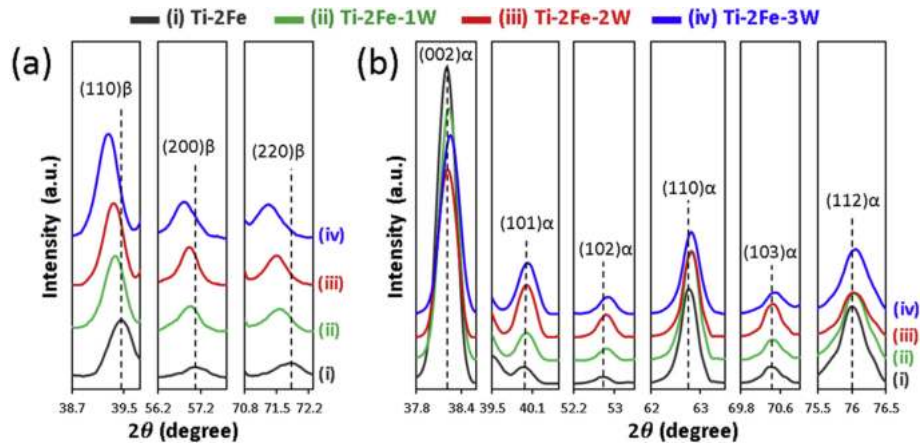
Fig. 7 − XRD diffraction pattern of extruded Ti−2Fe−(0−3)W alloys showing the main peaks of (a) β phase and (b) α phase separately. A clear peak shift is observed for the β-phase diffraction pattern.

globular α grains that are bonded continuously and arranged toward the extrusion direction (Figs. 3a and 4a). The kinking of α colonies has been described as an indication of globularization evolution in previous reports [17,21,29,30]. Shear bands are significantly activated as the kinks get sharper. That is, the kinking process is strongly associated with the development of shear bands within the α colonies. The progressive development of the shear bands within the kinking process of α colonies results in the significant breakage of β layers and, consequently, microstructure forms with low aspect ratios (globular) [31].

By introducing W solute, kinks were eliminated along with the slight refinement of α grains. The β phase fraction increased marginally in Ti−2Fe−1W; however, the microstructure was maintained in the equiaxed morphology (Figs. 3b and 4b). By adding more W (Ti−2Fe−2W), α phase morphology changed so that globular and partially acicular shapes formed with limited bonded-continuous grains, as shown in Figs. 3c and 4c. Finally, when W content increased to 3 wt%, the microstructure completely changed to a fully acicular α phase (Figs. 3d and 4d). Based on the β stabilizers and actual temperature of extrusion, different phases can exist during extrusion. In general, there is a temperature drop before extrusion when samples are removed from the furnace and placed into the die. According to [15], the temperature of specimens decreases about 200−300 °C during hot deformation which results in microstructure changes. Owing to the highest amount of β stabilizer elements, Ti−2Fe−3W probably was in the β region during extrusion. Immediately after extrusion, the β → α transformation takes place from the prior β grains leading to acicular α formation during cooling [32]. In contrast, Ti−2Fe−2W probably was in α+β during extrusion due to the lower β stabilizer elements. Acicular α changes to globularized during hot deformation, and the small amount of remaining metastable β transforms to α phase with acicular shape and grows larger. The α phase evolutions for extruded Ti−2Fe−2W and Ti−2Fe−3W alloys are illustrated schematically in Fig. 5.

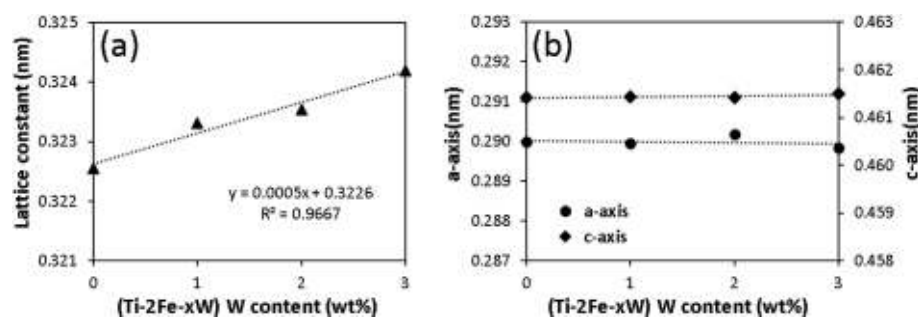| Table 1 − Detail of the diffraction peak shifts in the β phase.			
Material	β peak, 2θ (degree)		
	110	200	220
Ti−2Fe	39.414	57.080	71.801
Ti−2Fe−1W	39.327	56.893	71.472
Ti−2Fe−2W	39.307	56.878	71.418
Ti−2Fe−3W	39.224	56.772	71.245

Fig. 8 − Lattice constant change in extruded Ti−2Fe−(0−3)W alloys in terms of W content (a) β phase (b) α phase.
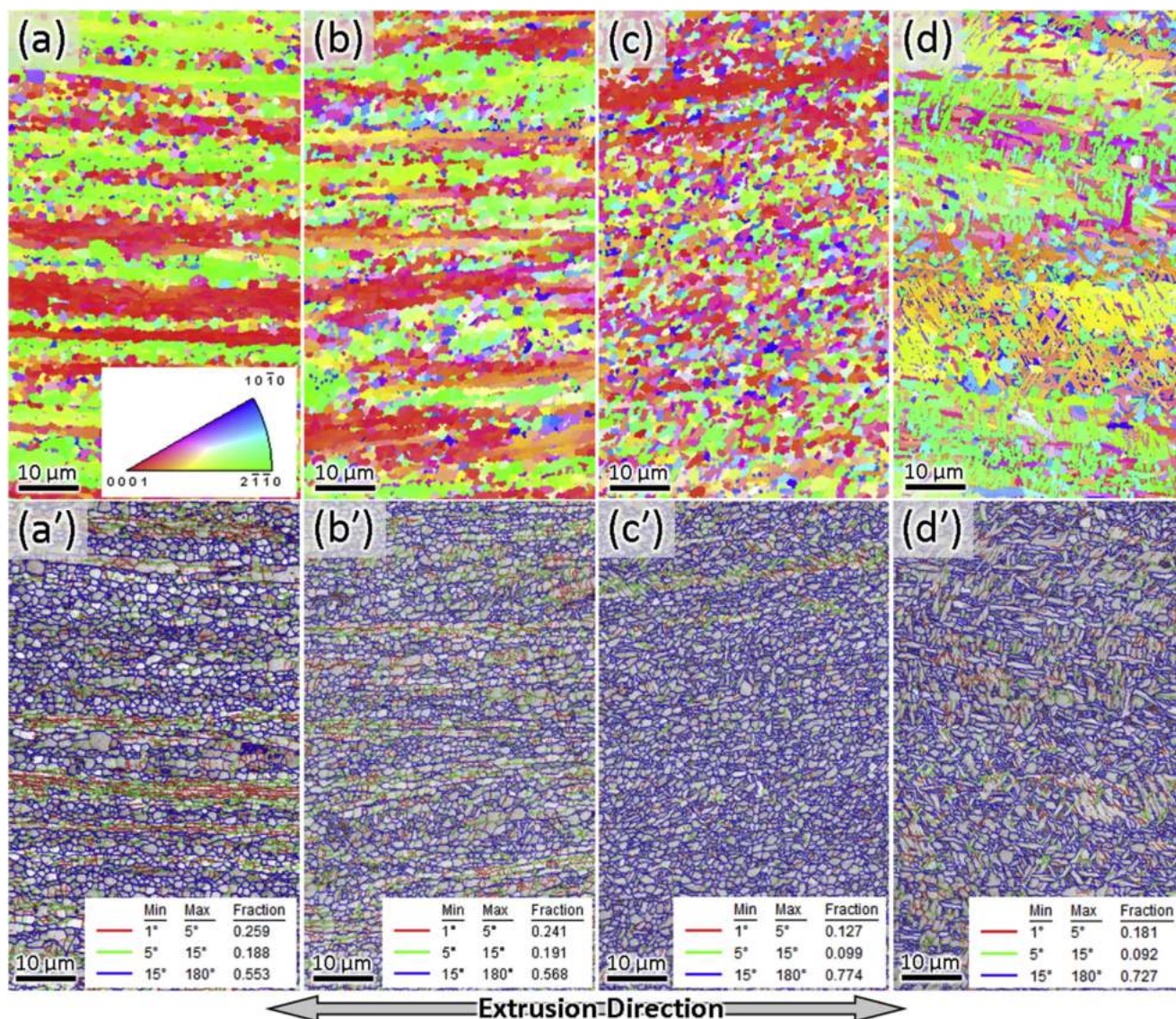
Fig. 9 — IPFs of extruded alloys — (a) Ti—2Fe, (b) Ti—2Fe—1W, (c) Ti—2Fe—2W, (d) Ti—2Fe—3W — and (a′—d′) corresponding IQ maps overlaid with grian boundaries.

In general, FESEM images show that fine-grain micro-structure was developed in all of the alloys regardless of the W content, which is attributed to the dynamic recrystallization during hot extrusion [17]. To study the distribution of alloying elements, EDS elemental mapping and point scanning were used. Fig. 6 shows the analysis of the results obtained from extruded Ti—2Fe—2W alloy. Point scanning of 1 and 2 show the formation of α-Ti, and 3 and 4 indicate the formation of β-Ti. According to the figure, Fe and W predominantly diffused into β-Ti, while their solution in the α-Ti was small. W content in α-Ti was expected to be lower than the obtained values because of the EDS measurement limitation and errors for scanning areas of <1 μm^2.

Fig. 7 shows the XRD analysis of extruded Ti—2Fe—(0—3)W alloys. XRD peak patterns of α and β phases are illustrated separately. The β peaks shifted towards lower diffraction angles (Table 1), while the α peaks remained almost un-changed. This behavior agrees with preferential diffusion of Fe and W in β due to their characteristic as eutectoid β stabi-lizer elements. The lattice constant can be calculated using peak shift applying Bragg's low [33]:

$$d = n\lambda/2sin\theta, \tag{1}$$

where d is the distance of crystal planes, n is a positive integer, λ is the wavelength of X-ray, and θ is the diffraction angle. Therefore, the lattice constant in body-centered cubic (bcc) and hexagonal closed-packed (hcp) can be determined by the following equations:

$$d = \sqrt{a^2 / \left(h^2 + k^2 + l^2\right)} \tag{2}$$
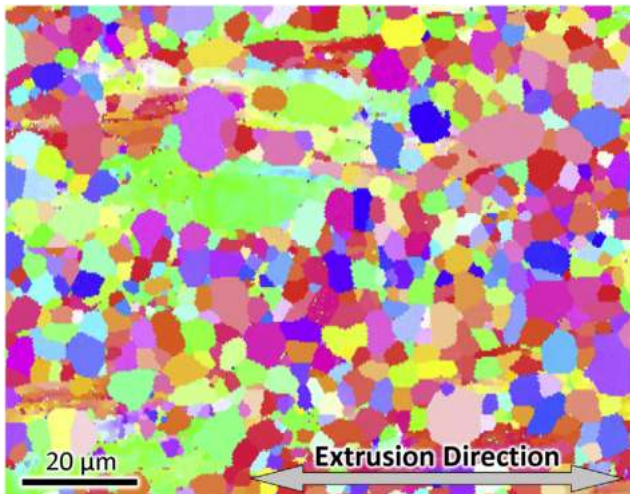
where a is the lattice constant in β-Ti for bcc, and

Fig. 10 – IPF of pure Ti extruded at 1000 °C as a reference material.

$$d = 1 \left/ \sqrt{4\left(h^2 + k^2 + hk\right)\left/3a^2 + l^2\right/c^2} \right. \qquad (3)$$

where a and c are the lattice constants of the a-axis and c-axis in α-Ti for hcp.

The calculated lattice constant of β-Ti is shown in Fig. 8a, where Ti–2Fe has the lowest value (0.3225 nm) and Ti–2Fe –3W has the highest value (0.3242 nm), showing a gradual increase in the lattice constant by 1 wt% W increment in Ti–2Fe matrix. This is an indication of crystal expansion due to the W solid solution. In contrast, lattice parameters of α-Ti measured as $a = 0.2901$ nm, $c = 0.4615$ nm, and $c/a = 1.591$, which is close to the standard values according to PDF card 00-0441294 for α-Ti ($c/a = 1.587$ nm). This implies that Fe and W solutes do not affect the lattice constants of α-Ti considerably, as depicted in Fig. 8b.

Fig. 9 shows the inverses pole figure (IPF) and image quality (IQ) maps overlaid with grian boundaries of extruded Ti–2Fe–(0–3)W alloys, while the IPF map of pure Ti is shown in Fig. 10 for reference; average grain size is 13 μm. Since the α phase is the main constituent, the color code of only the α phase is shown in the IPF map. The indices of a crystal face are identified as red, blue, and green, representing (0001), (10$\bar{1}$0), and (11$\bar{2}$0) crystal planes, respectively. The W addition affected recrystallization and grain orientation. Grain morphologies and grain boundary characteristics are shown in IQ maps. Low angle grain boundaries (LAGBs, $1° < \theta < 15°$) are illustrated with red and green lines, while blue lines represent high angle grain boundaries (HAGBs, $15° < \theta < 180°$). The figure shows that the addition of 1% of W solute caused no considerable change in the fraction of HAGBs. By contrast, increasing the amount of W solute increased the HAGBS significantly, and Ti–2Fe–2W showed a maximum fraction of approximately 77%.

The optical microscopy observation of the extruded Ti–2Fe–3W revealed the existence of some lines parallel to the extrusion direction. To identify and characterize these lines in detail, EBSD was conducted, and Fig. 11 shows that these lines represent the strongly oriented α grains, where basal planes are transverse to the extrusion direction, resulting in a sharp basal texture. This partially formed sharp texture could affect the mechanical properties of this material. Additionally, the grain boundary of this area was dominated by LAGBs ($5° < \theta < 15°$).

Fig. 12 shows the texture evaluation of extruded alloys using pole figure (PF) and triangle IPF maps. PF maps calculated in (0001) and (11$\bar{2}$0) planes show a fiber texter in Ti–2Fe and Ti–2Fe–1W, while the texture changed by increasing W in Ti–2Fe–2W and Ti–2Fe–3W alloys. The strong effect of W on the texture was clarified by triangle IPF maps. W reduced the intensity of prismatic texture (10$\bar{1}$0) greatly; in particular, Ti–2Fe–2W showed the lowest maximum intensity I_{max} among W-content alloys, approximately 20% that of Ti–2Fe. The (10$\bar{1}$0) plane is known to be the softest plane in hcp Ti crystal. Hence, this observation shows that the different crystal orientations in Ti–2Fe–2W can contribute to the strength along with other main factors such as grain size.
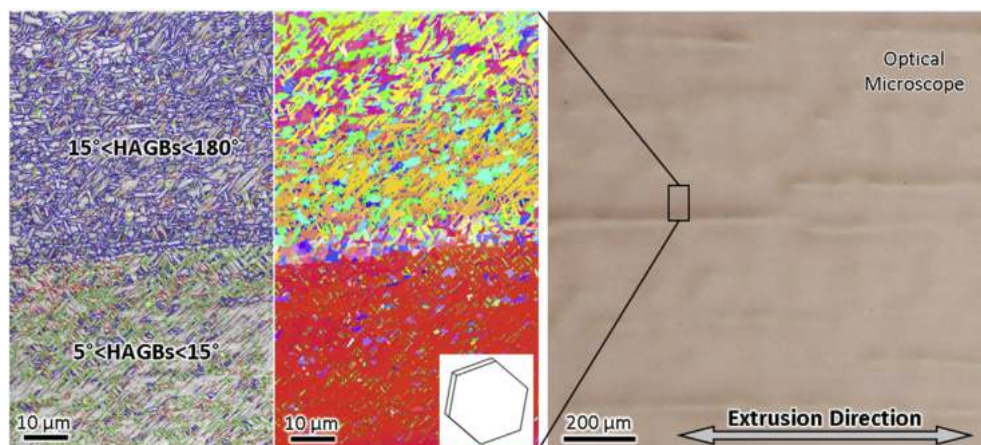

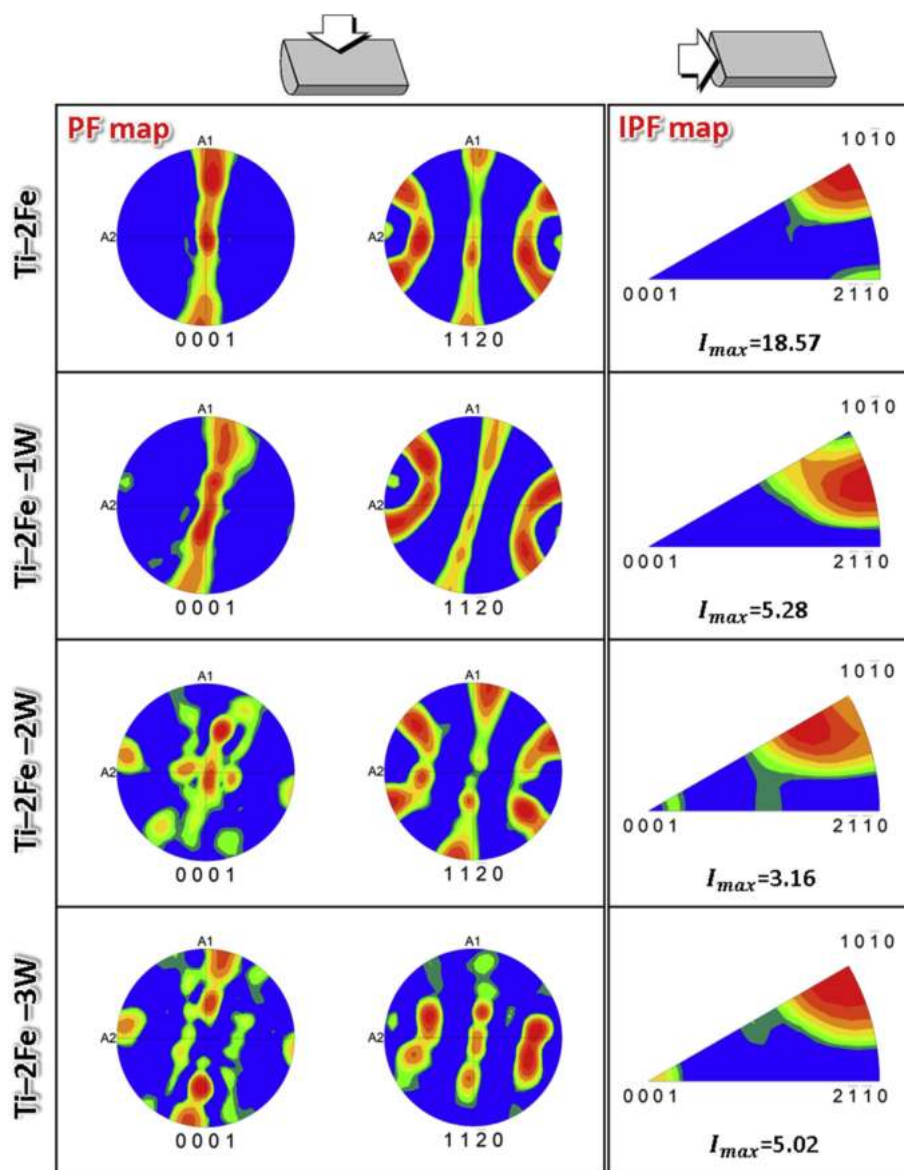**Fig. 11 – IPF and optical microscope observation of Ti–2Fe–3W.**

Fig. 12 — Texture evaluation of extruded Ti—2Fe—(0—3)W alloys by PF and triangle IPF maps.

Additionally, the EBSD evaluations using Orientation Imaging Microscopy (OIM) analysis, showed that the grain refinement occurred by adding W solute until 2%, where the smallest grain size (~1.64 μm) was observed in Ti—2Fe—2W. However, when W content was 3%, grain size increased to ~3.69 μm in Ti—2Fe—3W. Grain size is dependent on the recrystallization and the solute content. Generally, by increasing solute content, grain size decreases due to the solute drag effect [17,28]. Therefore, grain size decreased as W content increased to 2 wt%. But, as explained above (Fig. 5), the mechanism of α phase formation is different in Ti—2Fe—3W, resulting in larger/acicular shape formation compared to the other specimens. Similar microstructure evolution and grin size variation has been reported in the previous research on Ti—Fe alloys [32]. The summary of the microstructure analysis is given in Table 2. The W content materials showed almost

Table 2 — Summary of microstructure characteristics in Ti—2Fe—(0—3)W alloys extruded at 1000 °C.

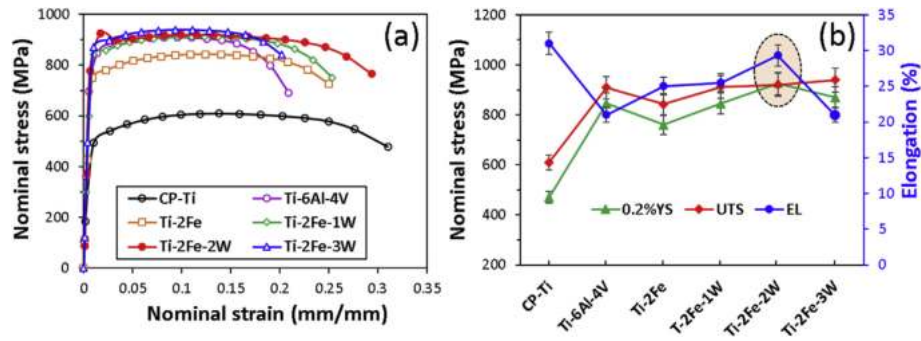| Material	Average grain size (μm)	α Grain morphology	α Phase fraction (vol %)	β Phase fraction (vol %)
Ti—2Fe	3.32	equiaxed	94.1	5.9
Ti—2Fe—1W	2.2	equiaxed	89.3	10.7
Ti—2Fe—2W	1.64	equiaxed + acicular	90.0	10.0
Ti—2Fe—3W	3.53	acicular	87	13.0

Fig. 13 – **(a) Nominal stress–strain curves of extruded Ti–2Fe–(0–3)W, Ti–6Al–4V and CP-Ti and (b) a summary of mechanical properties.**

similar α-phase fractions (~90%) as a predominant constituent. As is well accepted, constituent phases in two-phase Ti alloys not only depend on β-stabilizer alloying elements but also are affected by thermomechanical processing parameters, such as the temperature of hot deformation. Therefore, this effect needs to be considered during the hot extrusion at the β phase region by which the fraction of developed phases can be controlled when cooling and β→α transformation occurs. As a result, α grows according to the orientation relationship of Burgers vectors shown below [34].

$$\{110\}\beta \parallel (0001)\alpha$$

$$\left[1\bar{1}1\right]\beta \parallel \left[11\bar{2}0\right]\alpha$$

3.2. Evaluation of tensile properties

The nominal stress–strain curve of the extruded Ti–2Fe–(0–3)W alloys, Ti–6Al–4V, and pure Ti as reference material are illustrated in Fig. 13a. Ti–2Fe showed a remarkable increase in yield stress (760 MPa) compared to pure Ti (480 MPa), which was produced with a similar processing condition. The addition of W solute to Ti–2Fe matrix resulted in a different tensile behavior so that tensile yield strength gradually increased as W increased by 1 wt% and 2 wt% (845 MPa and 925 MPa, respectively), while both also showed adequate elongation (EL > 25%). Ti–2Fe–2W showed a drop after a sharp yielding, which is probably attributed to the

interaction between dislocation and fine α grains [35]. This behavior, also known as yield point phenomena, indicating discontinuous yielding (including upper and lower yield points) is associated with the pre-existing dislocations in the material that are not able to accommodate the strain in the early stages of yielding. This may be due to pinning of dislocations by the solute atoms. Hence, multiplication and activation of new sources of dislocations occur, and when stress increases up to a critical point, the flow stress abruptly degrades to the lower yield point by the movement of a large number of dislocations [36]. Ti–2Fe–3W demonstrated a slight reduction in yielding stress (870 MPa) and EL (21%) compared to Ti–2Fe–2W. Nevertheless, this EL is considered high, according to ASTM B348, particular, when compared with Ti grade 38, which can contain 1.8 wt% Fe [37].

This strengthening tendency is attributed to the microstructure characteristics. In comparison with CP-Ti, the strengthening of Ti–2Fe, Ti–2Fe–1W, and Ti–2Fe–2W is associated with the grain refinement and W solid solution. Ti–2Fe–2W presented not only the smallest median grain size and high W content but also comprised bimodal microstructure including acicular + globular α grains. Ti–2Fe–3W, which contained the maximum W solute and consisted of fully coarse acicular α grain, demonstrated the lowest tensile yield strength, owing to acicular α grains' having less contribution to the room temperature tensile strength compared to globularized morphology [4]. The obtained mechanical properties, namely 0.2% yield strength (YS), ultimate tensile
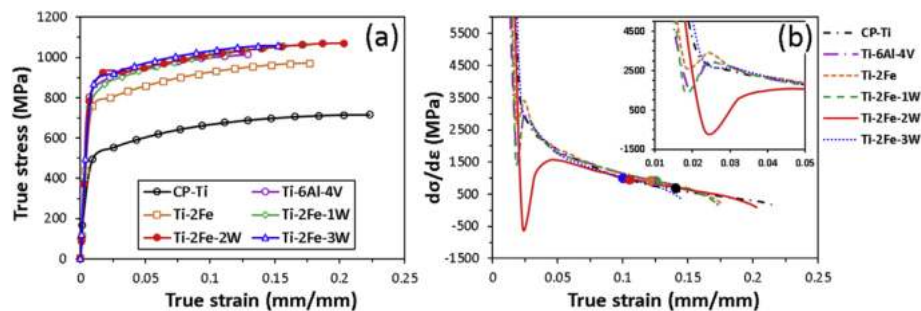

Fig. 14 – **(a) True stress–strain curves and (b) work hardening evaluations of extruded Ti–2Fe–(0–3)W, Ti–6Al–4V and CP-Ti.**
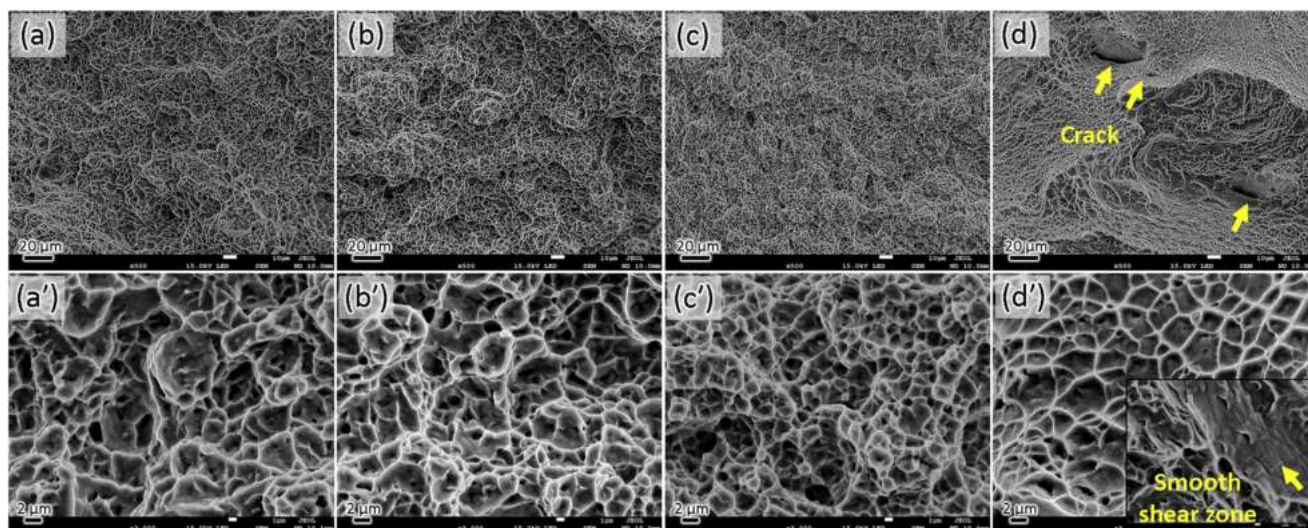
Fig. 15 — Typical surface fracture of extruded materials after tensile test including different magnification (a, a′) Ti—2Fe (b, b′) Ti—2Fe—1W (c, c′) Ti—2Fe—2W (d, d′) Ti—2Fe—3W.

strength (UTS), and EL, are summarized in Fig. 13b. As highlighted, Ti—2Fe—2W showed the best mechanical properties in terms of 0.2%YS, UTS, and EL, which is comparable with Ti—6Al—4V. This implies that our developed low-cost alloy with small amounts of elements can exhibit improved mechanical properties compared with conventional Ti—6Al—4V containing rather expensive alloying elements.

Fig. 14 illustrates the true stress—strain curves and corresponding strain hardening $(d\sigma/d\varepsilon)$ evaluations of Ti—2Fe—(0—3) W alloys, along with CP—Ti and Ti—6Al—4V. The necking point of each material was marked by colored circles that represent true strain values of necking that were calculated based on Considère's criterion [38] ($\Theta = 1/\sigma(\Delta\sigma/\Delta\varepsilon) \leq 1$, where Θ is the normalized strain hardening and σ and ε are true stress and strain, respectively). Ti—2Fe—2W and

Ti—2Fe—3W exhibited lower uniform deformation by necking earlier than Ti—2Fe and Ti—2Fe—1W. The strain hardening behavior of these investigated materials can be divided into separate steps. In the first step, all materials showed high strain hardening that declined sharply and the alloy with 2W reached the lowest strain hardening. Next, the Ti—2Fe—(0-2) W and Ti—6Al—4V showed a rise in the strain hardening before reaching the third step. This behavior in Ti alloys is associated with the effect of solution elements, which was described in a previous report [39]. However, such behavior in the material containing 3W was marginal. Finally, the strain hardening decreased slowly, where a trade-off in dislocation generation and annihilation governs the $d\sigma/d\varepsilon$. Interestingly, the strain hardening behavior of Ti—2Fe—1W was completely overlapped with Ti—6Al—4V.
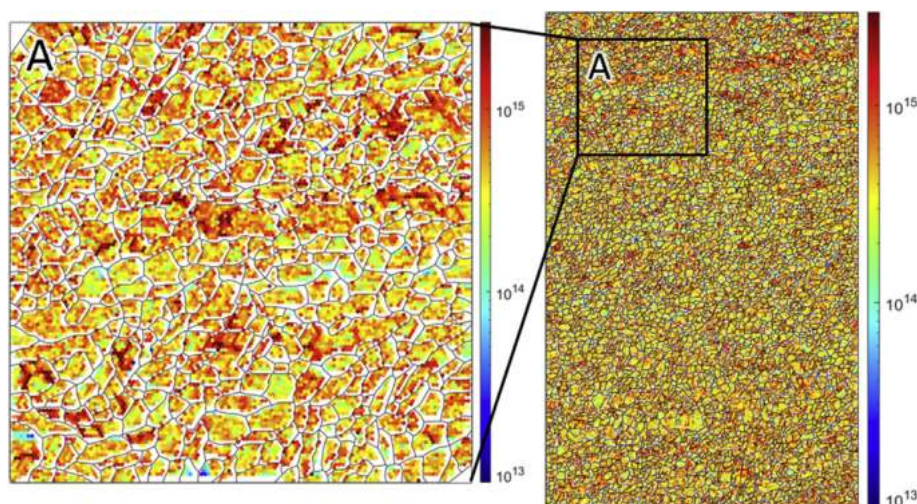

Fig. 16 — Distribution of GNDs in Ti—2Fe—2W including high magnification observation, which was calculated from EBSD.

The fractography of tensile specimens (Fig. 15) also presented a ductile fracture mode with finely dimpled morphology across the fracture surface. The size of the dimples matched with the grain size of extruded materials, where Ti−2Fe−2W had the most refined dimple fracture surface. Additionally, some micro-cracks, along with smooth shear zones, were observed in Ti−2Fe−3W, which could be another reason for yielding at lower strength during tensile loading.

3.3. Quantitative analysis of strengthening factors

Considering the excellent trade-off in tensile strength and elongation, as-extruded Ti−2Fe−2W exhibited the highest yield point, approximately 925 MPa, indicating a 445 MPa increase in the YS compared to CP-Ti. Therefore, Ti−2Fe−2W was selected as an optimized composition of our study in order to clarify the underlying strengthening mechanisms. The metallic materials are generally strengthened by solid solution, grain refinement, dislocation density, and particle reinforcement. In this research, we ignored the effect of reinforcements because no precipitation was observed. Solid solution strengthening could be considered only for the β phase because Fe and W as β stabilizers have limited diffusion in the α phase. The strengthening was evaluated using the model developed by Gypen [40] and Toda-Caraballo [41] for multicomponent alloys:

$$\Delta\sigma_{SS} = \left(\sum_i B_i^{3/2} X_i\right)^{2/3} \tag{4}$$

where B_i is strengthening factor and X_i is the solution element in the atomic fraction. The values of B_i for Fe and W were calculated as 1715 and 574, respectively [42]. Therefore, the contribution of the solid solution on the strengthening of Ti−2Fe−2W was determined as 133 MPa.

The extrusion of Ti alloys resulted in considerable grain refinement, owing to dynamic recrystallization. The grain refinement increased the density of grain boundaries which hindered the dislocation mobility, consequently contributing to the material strengthening. The YS increment by grain refinement could be estimated using Hall−Petch relation described as follows [43]:

$$\Delta\sigma_{GR} = K\left(d_2^{-0.5} - d_1^{-0.5}\right) \tag{5}$$

where K is a constant on the order of 0.4 MPa $\sqrt{m}$ [44] for Ti, and d_1 (13 μm) and d_2 (1.64 μm) are the average grain sizes before and after grain refinement, respectively. Hence, this calculation shows that grain refinement improved the strength by 202 MPa.

Dislocations are generated during plastic deformation and interact with each other, such that the obstruction of the dislocation movement by stress field formation results in strength improvement. The relationship between dislocation density and increment in the YS is described by Bailey−Hirsch [45]:

$$\Delta\sigma_D = M\alpha Gb\sqrt{\rho} \tag{6}$$

where M is Taylor factor (α-Ti: 0.85, β-Ti: 2.8 [42]), α is a constant (α-Ti: 0.2, β-Ti: 0.3 [46,47]), G is the shear modulus (α-Ti: 45.6 GPa, β-Ti: 36 GPa [48,49]), b is the Burgers vector (α-Ti: 0.295 nm, β-Ti: 0.254 nm [50]), and ρ is the dislocation density.

The dislocation density stored in a crystal during a given strain history is the sum of the geometrically necessary dislocations (GNDs) and the statistically-stored dislocations (SSDs). An SSD is a characteristic of the material (crystal structure, shear modulus, stacking-fault energy, etc.), while GND is a characteristic of the microstructure (the geometric arrangement and size of grains and phases) that is considered independent of the material [51]. The GND density ρ_{GND} is related to the local strain gradient field and develops as a result of lattice curvature and rotation due to plastic deformation [52]. In the ultrafine-grained materials, ρ_{GND} is significantly larger than SSDs density ρ_{SSD}. Additionally, GNDs are responsible for about 90% of total dislocations in severely deformed materials. According to Ashby's hardening [51], wherever nonuniform plastic deformation occurs, the ρ_{GND} is increased, whereby GNDs act as obstacles to dislocation movement and enhance hardening. That is, the main contribution to the strength of dislocation density is attributed to GNDs [53]. Therefore, ρ_{GND} is evaluated to estimate the strengthening effect in Eq. (6).

In this work, the GNDs were computed considering the curvature components of the lattice tensor. The method used in this work, which allows for the estimation of GNDs from EBSD maps, is described in detail in [54]. The mathematical modeling was implemented in Matlab 2019 using the MTEX routine [55]. A cut-off misorientation angle of <5° was imposed. The calculated values of ρ_{GND} in α-Ti and β-Ti were 3.48×10^{14} m^{-2} and 5.99×10^{14} m^{-2}, respectively, which increased the yield strength by approximately 65 MPa. The map distribution of GNDs obtained from EBSD is illustrated in Fig. 16. Of note, the dislocations in this map are spread uniformly over the entire grain for the most deformed grain. Considering the above operating strengthening factors, the total strength increment can be estimated by Eq. (7):

$$\Delta\sigma_y = \left(\sum_i B_i^{3/2} X_i\right)^{2/3} + K\left(d_2^{-0.5} - d_1^{-0.5}\right) + M\alpha Gb\sqrt{\rho} \tag{7}$$

Therefore, the total increment in the YS was calculated as 400 MPa, which matched well with the 445 MPa strength increment observed in the experimental evaluations. Based on the quantitative analysis, grain refinement, Fe and W solid solution, and GNDs have the highest strengthening effects, respectively.

4. Conclusion

Thermomechanical treatment and solid solution are well known to greatly improve the mechanical properties of metallic materials. In this research, we present a novel approach in the strengthening of Ti−Fe alloying, using a complete solid solution of W and employing hot extrusion at high temperature (1000 °C). Microstructure observations

revealed that the extruded Ti—2Fe—(0—3)W materials mainly consisted of α-phase, whereas the morphologies were different. The equiaxed α grains were formed in Ti—2Fe and Ti—2Fe—1W, while Ti—2Fe—2W and Ti—2Fe—3W indicated equiaxed + acicular and acicular shape, respectively. Ti—2Fe—(0—3)W alloys exhibited a remarkable balance in strength—ductility, in particular, Ti—2Fe—2W, which revealed the smallest grain size (~1.64 μm) and highest yield strength of 925 MPa and elongation of 30%. Hence, Ti—2Fe—2W was selected as the optimized composition in our study. Strengthening was analyzed quantitatively in Ti—2Fe—2W considering possible strengthening factors, such as grain refinement, solid solution, and GNDs. Because of the extrusion at high temperature, the effect of GNDs was the least among other operating factors, while grain refinement effectively increased the yield stress. Finally, the quantitative analysis of strengthening aligned well with the obtained experimental results.

Declaration of Competing Interest

The authors declare that they have no known competing financial interests or personal relationships that could have appeared to influence the work reported in this paper.

Acknowledgments

REFERENCES

[1] de Castro V, Leguey T, Muñoz A, Monge MA, Pareja R. Microstructure and tensile properties of Y_2O_3-dispersed titanium produced by arc melting. Mater Sci Eng A 2006;422:189—97. https://doi.org/10.1016/j.msea.2006.02.027.

[2] Issariyapat A, Visuttipitukul P, Song T, Bahador A, Umeda J, Qian M, et al. Tensile properties improvement by homogenized nitrogen solid solution strengthening of commercially pure titanium through powder metallurgy process. Mater Charact 2020;170:110700. https://doi.org/10.1016/j.matchar.2020.110700.

[3] Li S, Kondoh K, Imai H, Chen B, Jia L, Umeda J. Microstructure and mechanical properties of P/M titanium matrix composites reinforced by in-situ synthesized TiC-TiB. Mater Sci Eng A 2015;628:75—83. https://doi.org/10.1016/j.msea.2015.01.033.

[4] Bahador A, Umeda J, Yamanoglu R, Abu Bakar TA, Kondoh K. Strengthening evaluation and high-temperature behavior of Ti—Fe—O—Cu—Si alloy. Mater Sci Eng A 2021;800:140324. https://doi.org/10.1016/j.msea.2020.140324.

[5] Hu Y, Zhao B, Ning F, Wang H, Cong W. In-situ ultrafine three-dimensional quasi-continuous network microstructural TiB reinforced titanium matrix composites fabrication using laser engineered net shaping. Mater Lett 2017;195:116—9. https://doi.org/10.1016/j.matlet.2017.02.112.

[6] Gorsse S, Chaminade JP, Le Petitcorps Y. In situ preparation of titanium base composites reinforced by TiB single crystals using a powder metallurgy technique. Compos Part A Appl Sci Manuf 1998;29:1229—34. https://doi.org/10.1016/S1359-835X(98)00080-3.

[7] Kondoh K, Sun B, Li S, Imai H, Umeda J. Experimental and theoretical analysis of nitrogen solid-solution strengthening of PM Titanium. Int J Powder Metall 2014;50:35—40.

[8] Veiga C, Loureiro AJR, Davim JP. Properties and applications of titanium alloys. Rev Adv Mater Sci 2012;32:133—48.

[9] Milošev I, Žerjav G, Calderon Moreno JM, Popa M. Electrochemical properties, chemical composition and thickness of passive film formed on novel Ti-20Nb-10Zr-5Ta alloy. Electrochim Acta 2013;99:176—89. https://doi.org/10.1016/j.electacta.2013.03.086.

[10] Kariya S, Fukuo M, Umeda J, Kondoh K. Quantitative analysis on light elements solution strengthening in pure titanium sintered materials by labusch model using experimental data. Mater Trans 2019;60:263—8. https://doi.org/10.2320/matertrans.Y-M2018849.

[11] Mimoto T, Umeda J, Kondoh K. Strengthening behaviour and mechanisms of extruded powder metallurgy pure ti materials reinforced with ubiquitous light elements. Powder Metall 2016;59:223—8. https://doi.org/10.1080/00325899.2016.1148847.

[12] Ye XX, Imai H, Shen JH, Chen B, Han GQ, Umeda J, et al. Dynamic recrystallization behavior and strengthening-toughening effects in a near-α Ti-xSi alloy processed by hot extrusion. Mater Sci Eng A 2017;684:165—77. https://doi.org/10.1016/j.msea.2016.12.054.

[13] Yang Y, Chen RR, Fang HZ, Guo JJ, Ding HS, Su YQ, et al. Improving microstructure and mechanical properties of $Ti_{43}Al_5Nb0._1B$ alloy by addition of Fe. Rare Met 2019;38:1024—32. https://doi.org/10.1007/s12598-019-01208-3.

[14] Bahador A, Kariya S, Umeda J, Hamzah E, Kondoh K. Tailoring microstructure and properties of a superelastic Ti—Ta alloy by incorporating spark plasma sintering with thermomechanical processing. J Mater Eng Perform 2019;28:3012—20. https://doi.org/10.1007/s11665-019-04061-8.

[15] Bahador A, Hamzah E, Kondoh K, Abu Bakar TA, Yusof F, Imai H, et al. Effect of deformation on the microstructure, transformation temperature and superelasticity of Ti—23 at% Nb shape-memory alloys. Mater Des 2017;118:152—62. https://doi.org/10.1016/j.matdes.2016.12.048.

[16] Yi X, Wang H, Sun B, Sun K, Huang C, Gao Z, et al. The microstructural characteristics and high temperature mechanical properties of quaternary Ti—V—Al—Co shape memory alloys. J Alloys Compd 2020;835:155416. https://doi.org/10.1016/j.jallcom.2020.155416.

[17] Bahador A, Umeda J, Ghandvar H, Asma T, Bakar A, Yamanoglu R, et al. Microstructure globalization of high oxygen concentration dual-phase extruded Ti alloys via powder metallurgy route. Mater Charact 2021;172:110855. https://doi.org/10.1016/j.matchar.2020.110855.

[18] Lütjering G. Influence of processing on microstructure and mechanical properties of (α + β) titanium alloys. Mater Sci Eng A 1998;243:32—45. https://doi.org/10.1016/s0921-5093(97)00778-8.

[19] Gao P, Yang H, Fan X, Zhu S. Unified modeling of flow softening and globularization for hot working of two-phase titanium alloy with a lamellar colony microstructure. J Alloys Compd 2014;600:78—83. https://doi.org/10.1016/j.jallcom.2014.02.110.

[20] Oh JM, Park CH, Yeom JT, Hong JK, Kang N, Lee SW. High strength and ductility in low-cost Ti—Al—Fe—Mn alloy exhibiting transformation-induced plasticity. Mater Sci Eng A 2020;772:138813. https://doi.org/10.1016/j.msea.2019.138813.

[21] Bieler TR, Semiatin SL. The origins of heterogeneous deformation during primary hot working of Ti-6Al-4V. Int J Plast 2002;18:1165—89. https://doi.org/10.1016/S0749-6419(01)00057-2.

[22] Imayev V, Gaisin R, Rudskoy A, Nazarova T, Shaimardanov R, Imayev R. Extraordinary superplastic properties of hot worked Ti-45Al-8Nb-0.2C alloy. J Alloys Compd 2016;663:217—24. https://doi.org/10.1016/j.jallcom.2015.11.228.

[23] Semiatin SL, Seetharaman V, Weiss I. Flow behavior and globularization kinetics during hot working of Ti-6Al-4V with a colony alpha microstructure. Mater Sci Eng A 1999;263:257—71. https://doi.org/10.1016/s0921-5093(98)01156-3.

[24] Zhang H, Feng P, Akhtar F. Aluminium matrix tungsten aluminide and tungsten reinforced composites by solid-state diffusion mechanism. Sci Rep 2017;7:1—8. https://doi.org/10.1038/s41598-017-12302-w.

[25] Frary M, Abkowitz S, Abkowitz SM, Dunand DC. Microstructure and mechanical properties of Ti/W and Ti-6A1-4V/W composites fabricated by powder-metallurgy. Mater Sci Eng A 2003;344:103—12. https://doi.org/10.1016/S0921-5093(02)00426-4.

[26] Maji P, Dube RK, Basu B. Enhancement of wear resistance of copper with tungsten addition ($\leq$20 wt %) by powder metallurgy route. J Tribol 2009;131:1—9. https://doi.org/10.1115/1.3204776.

[27] Wei Q, Kecskes LJ. Effect of low-temperature rolling on the tensile behavior of commercially pure tungsten. Mater Sci Eng A 2008;491:62—9. https://doi.org/10.1016/j.msea.2008.01.013.

[28] Bahador A, Umeda J, Yamanoglu R, Amrin A, Alhazaa A, Kondoh K. Ultrafine-grain formation and improved mechanical properties of novel extruded Ti-Fe-W alloys with complete solid solution of tungsten. J Alloys Compd 2021;875:160031. https://doi.org/10.1016/j.jallcom.2021.160031.

[29] Seshacharyulu T, Medeiros SC, Morgan JT, Malas JC, Frazier WG, Prasad YVRK. Hot deformation and microstructural damage mechanisms in extra-low interstitial (ELI) grade Ti-6Al-4V. Mater Sci Eng A 2000;279:289—99. https://doi.org/10.1016/S0921-5093(99)00173-2.

[30] Park CH, Park KT, Shin DH, Lee CS. Microstructural mechanisms during dynamic globularization of Ti-6A1-4V alloy. Mater Trans 2008;49:2196—200. https://doi.org/10.2320/matertrans.L-MRA2008832.

[31] Mironov S, Murzinova M, Zherebtsov S, Salishchev GA, Semiatin SL. Microstructure evolution during warm working of Ti-6Al-4V with a colony-α microstructure. Acta Mater 2009;57:2470—81. https://doi.org/10.1016/j.actamat.2009.02.016.

[32] Umeda J, Tanaka T, Teramae T, Kariya S, Fujita J. Microstructures analysis and quantitative strengthening evaluation of powder metallurgy Ti—Fe binary extruded alloys with (α+β)-dual-phase. Mater Sci Eng A 2021;803:140708. https://doi.org/10.1016/j.msea.2020.140708.

[33] Sun B, Li S, Imai H, Mimoto T, Umeda J, Kondoh K. Fabrication of high-strength Ti materials by in-process solid solution strengthening of oxygen via P/M methods. Mater Sci Eng A 2013;563:95—100. https://doi.org/10.1016/j.msea.2012.11.058.

[34] Savage MF, Tatalovich J, Zupan M, Hemker KJ, Mills MJ. Deformation mechanisms and microtensile behavior of single colony Ti-6242Si. Mater Sci Eng A 2001;319—321:398—403. https://doi.org/10.1016/S0921-5093(01)01024-3.

[35] Li Z, Fu L, Fu B, Shan A. Yield point elongation in fine-grained titanium. Mater Lett 2013;96:1—4. https://doi.org/10.1016/j.matlet.2012.12.115.

[36] Momeni A, Abbasi SM, Morakabati M, Akhondzadeh A. Yield point phenomena in TIMETAL 125 beta Ti alloy. Mater Sci Eng A 2015;643:142—8. https://doi.org/10.1016/j.msea.2015.07.031.

[37] ASTM B348. Standard specification for titanium and titanium alloy bars and billets. ASTM International; 2009. p. 1—8.

[38] Bahador A, Umeda J, Yamanoglu R, Ghandvar H. Deformation mechanism and enhanced properties of Cu-TiB$_2$ composites evaluated by the in-situ tensile test and microstructure characterization. J Alloys Compd 2020;847:156555. https://doi.org/10.1016/j.jallcom.2020.156555.

[39] Shen J, Chen B, Umeda J, Zhang J, Li Y, Kondoh K. Rate sensitivity and work-hardening behavior of an advanced Ti-Al-N alloy under uniaxial tensile loading. Mater Sci Eng A 2019;744:630—7. https://doi.org/10.1016/j.msea.2018.12.066.

[40] Gypen LA, Deruyttere A. Multi-component solid solution hardening. J Mater Sci 1977;12:1034—8. https://doi.org/10.1007/bf00540988.

[41] Toda-Caraballo I, Rivera-Díaz-Del-Castillo PEJ. Modelling solid solution hardening in high entropy alloys. Acta Mater 2015;85:14—23. https://doi.org/10.1016/j.actamat.2014.11.014.

[42] Zhao GH, Liang XZ, Kim B, Rivera-Díaz-del-Castillo PEJ. Modelling strengthening mechanisms in beta-type Ti alloys. Mater Sci Eng A 2019;756:156—60. https://doi.org/10.1016/j.msea.2019.04.027.

[43] Shen J, Chen B, Umeda J, Kondoh K. Advanced mechanical properties of a powder metallurgy Ti-Al-N alloy doped with ultrahigh nitrogen concentration. JOM 2018;70:626—31. https://doi.org/10.1007/s11837-018-2780-9.

[44] Guo Y, Britton TB, Wilkinson AJ. Slip band-grain boundary interactions in commercial-purity titanium. Acta Mater 2014;76:1—12. https://doi.org/10.1016/j.actamat.2014.05.015.

[45] Bailey JE, Hirsch PB. The dislocation distribution, flow stress, and stored energy in cold-worked polycrystalline silver. Philos Mag 1960;5:485—97. https://doi.org/10.1080/14786436008238300.

[46] Dyakonov GS, Mironov S, Semenova IP, Valiev RZ. Chapter 7 - strengthening mechanisms and super-strength of severely deformed titanium. In: Garbacz H, Semenova IP, Zherebtsov S, Motyka M, editors. Nanocrystalline titanium. Elsevier; 2019. p. 123—43. https://doi.org/10.1016/B978-0-12-814599-9.00007-9.

[47] Gazder AA, Vu VQ, Saleh AA, Markovsky PE, Ivasishin OM, Davies CHJ, et al. Recrystallisation in a cold drawn low cost beta titanium alloy during rapid resistance heating. J Alloys Compd 2014;585:245—59. https://doi.org/10.1016/j.jallcom.2013.09.122.

[48] Gao J, Huang Y, Guan D, Knowles AJ, Ma L, Dye D, et al. Deformation mechanisms in a metastable beta titanium twinning induced plasticity alloy with high yield strength and high strain hardening rate. Acta Mater 2018;152:301—14. https://doi.org/10.1016/j.actamat.2018.04.035.

[49] Luo P, McDonald DT, Zhu SM, Palanisamy S, Dargusch MS, Xia K. Analysis of microstructure and strengthening in pure titanium recycled from machining chips by equal channel angular pressing using electron backscatter diffraction. Mater Sci Eng A 2012;538:252—8. https://doi.org/10.1016/j.msea.2012.01.039.

[50] Zhan H, Wang G, Kent D, Dargusch M. The dynamic response of a metastable β Ti-Nb alloy to high strain rates at room and elevated temperatures. Acta Mater 2016;105:104—13. https://doi.org/10.1016/j.actamat.2015.11.056.

[51] Ashby MF. The deformation of plastically non-homogeneous materials. Philos Mag 1970;21:399—424. https://doi.org/10.1080/14786437008238426.

[52] Arsenlis A, Parks DM. Crystallographic aspects of geometrically-necessary and statistically-stored dislocation density. Acta Mater 1999;47:1597—611. https://doi.org/10.1016/S1359-6454(99)00020-8.

[53] Li X, Sun BH, Guan B, Jia YF, Gong CY, Zhang XC, et al. Elucidating the effect of gradient structure on strengthening mechanisms and fatigue behavior of pure titanium. Int J Fatigue 2021;146:106142. https://doi.org/10.1016/j.ijfatigue.2021.106142.

[54] Pantleon W. Resolving the geometrically necessary dislocation content by conventional electron backscattering diffraction. Scr Mater 2008;58:994—7. https://doi.org/10.1016/j.scriptamat.2008.01.050.

[55] https://mtex-toolbox.github.io/.